Estimation of current constriction losses via 3D tomography reconstructions in electrochemical devices: a case study of a solid oxide cell electrode/electrolyte interface

Nielsen, Jimmi; Jørgensen, Peter Stanley

Published in:
Electrochimica Acta

Link to article, DOI:
10.1016/j.electacta.2017.08.100

Publication date:
2017

Document Version
Peer reviewed version

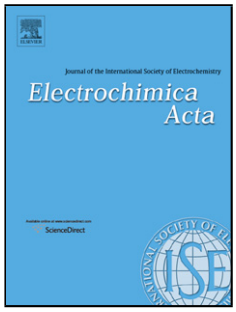

Title: Estimation of current constriction losses via 3D tomography reconstructions in electrochemical devices: a case study of a solid oxide cell electrode/electrolyte interface

Authors: Jimmi Nielsen, Peter Stanley Jørgensen

PII: S0013-4686(17)31742-5
DOI: http://dx.doi.org/10.1016/j.electacta.2017.08.100
Reference: EA 30104

To appear in: *Electrochimica Acta*

Received date: 22-5-2017
Revised date: 31-7-2017
Accepted date: 15-8-2017

Please cite this article as: Jimmi Nielsen, Peter Stanley Jørgensen, Estimation of current constriction losses via 3D tomography reconstructions in electrochemical devices: a case study of a solid oxide cell electrode/electrolyte interface, Electrochimica Actahttp://dx.doi.org/10.1016/j.electacta.2017.08.100

Estimation of current constriction losses via 3D tomography reconstructions in electrochemical devices: a case study of a solid oxide cell electrode/electrolyte interface

Jimmi Nielsen, Peter Stanley Jørgensen

Department of Energy Conversion & Storage, Technical University of Denmark, DK-4000 Roskilde, Denmark.

Abstract:

In the present study, the methodology for accurate estimations of the current constriction resistance in solid state electrochemical devices via 3D tomography reconstructions is developed. The methodology is used to determine the current constriction resistances at the Ni:YSZ anode / YSZ electrolyte interface of a solid oxide fuel cell. The current constriction at this interface becomes increasingly important as thinner electrolyte layers are continuously being pursued for increased performance. Various possible scenarios have been illustrated on idealized geometries as a function of electrolyte thicknesses, from which it is clear, that for a given set of electrodes an optimal electrolyte thickness exist. Thus, increased performance by reduction of the electrolyte thickness is only feasible down to a certain thickness, after which, a lower performance is obtained on a further reduction of the electrolyte thickness. The obtained results on current constriction resistances from numerical calculations on a 3D reconstruction of a Ni:YSZ anode / YSZ electrolyte assembly is compared with existing models with analytical expressions. The comparison shows, that the assumptions of existing models are by far too simple and the models are therefore not applicable for technological relevant electrochemical devices.

Keywords: current constriction, thin electrolyte, 3D reconstructions, SOFC, SOEC

1. Introduction

Electrochemical devices such as batteries, fuel cells, electrolysers, electrochemical reactors and electrochemical sensors are important technologies for the present and future society. To further improve or mature these technologies it is important to understand and characterize the different losses within the devices.

The present paper deals with estimation of current constriction losses within electrochemical devices. As a case study the current constriction losses of a solid oxide fuel cell (SOFC) anode / electrolyte interface is examined. Historically the first generation of SOFC was mechanically electrolyte supported. In order to be able to reduce the electrolyte thickness and

thus improve performance, the second generation anode supported solid oxide fuel cell (AS-SOFC) was developed. Today's state-of-the-art AS-SOFC have an electrolyte thickness of approximately 10 μm. Efforts are currently being made to reduce the electrolyte thickness further to achieve even higher performance [1-7]. As the electrolyte thickness is decreased the effect of current constriction resistance becomes more important. Furthermore, as will be evident from the present study a further reduction in the electrolyte layer thickness may have its limitations. It can in fact lead to an increase in resistance due to the onset of lateral currents within the electrolyte layer. The magnitude of the current constriction resistance of the individual electrode/electrolyte assemblies and the optimum electrolyte thickness depend on the structural characteristics of the electrodes. Attempts at quantifying the current constriction resistance have previously been made and models have been developed, which assume a uniformly distributed array of contact points either as squares or circles [8-9]. However, this is often not a good assumption as the electrode/electrolyte interfaces are much more complex. First of all, the electrode and electrolyte interface is not a plane in 3D nor is the electrode and electrolyte transition infinitely sharp. Secondly, the contact points are neither squares nor circles and they are not perfectly aligned on a grid. The aim of the present study is therefore to use 3D tomography electrode/electrolyte interfacial reconstructions in numerical Finite-Element-Method (FEM) calculations to get more accurate estimations of the current constriction resistance and the effect of varying the electrolyte thickness. In the present paper we report on the developed methodology for doing such calculations. First existing simplified analytical models and the situation present in a Ni:YSZ SOFC anode are presented. This is followed by experimental details concerning the sample examined and the numerical calculations performed. Hereafter results are presented, which first treats the situation of artificial ideal geometries, where an overview and interpretation of the different possible scenarios are provided. Finally, results and interpretation of a technological relevant conventional Ni:YSZ microstructured SOFC anode and YSZ electrolyte assembly is presented.

2. Theory

2.1 Existing models

For the description of the current constriction resistance originating from the discrete points between porous electrode and dense electrolyte layers, the following two models depicted in figure 1 has previously been developed. The models assume either contact points arranged as a regular array of squares or discs. The two models on current constriction resistance have been applied and used as explanation for why the observed conductivity of a reactive DC sputtered thin film had a four times lower conductivity than bulk YSZ [10]. In this work, the incomplete contact of the used Ag paste/YSZ film interface was believed to be the main reason for the

measured low conductivity of the prepared thin YSZ films. The two models have also been used for discussions on geometrical constraint in micro-SOFCs [11].

2.1.1 Model of Kenjo and Nakagawa (model a)

The model assumes contact points arranged as a regular array of squares as depicted in figure 1a. The ratio between effective resistance R_{eff} (with constriction) and the theoretical resistance R_{theor} (no constriction) can be calculated from the following expression [8]:

$$\frac{R_{eff}}{R_{theor}} = 1 - \frac{4d_a}{\pi^2 rl}\sum_{n=1}^{\infty}\frac{(-1)^n}{n^2} sin\left(n\pi(1-r)\right) tanh\left(\frac{\pi n l}{d_a}\right) \quad (1)$$

$$+\frac{4d_a}{\pi^3 r^2 l}\sum_{n=1}^{\infty}\sum_{m=1}^{\infty}\frac{(-1)^{n+m}}{nm\sqrt{n^2+m^2}} \times sin\left(n\pi(1-r)\right)sin\left(m\pi(1-r)\right) \times tanh\left(\frac{\pi\sqrt{n^2+m^2}\,l}{d_a}\right)$$

Where $r=(\Delta_a/d_a)$ and l is the thickness of the electrolyte layer. Δ_a is width of the contact points and d_a is the distance between the centers of the contact points as illustrated in figure 1a.

2.1.2 Model of Fleig and Maier (model b)

The model assumes contact points arranged as a regular array of disks as depicted in figure 1b. Here the overall resistance R_t is the sum of two contributions [9]:

$$R_t = R_1 + R_2 \quad (2)$$

R_1 is the theoretical resistance (no constriction) and R_2 is the additional resistance originating from the current constriction. R_2 could be described by the following relation:

$$R_2 = \rho\frac{f_{geo}}{2\Delta_b}\frac{1}{n} \quad (3)$$

Where ρ is the specific resistance of the electrolyte, Δ_b is the contact diameter and n is the number of contact disks. f_{geo} is a geometrical factor, which was estimated to be:

$$f_{geo} \approx \frac{1-\frac{\Delta_b}{d_b}}{1+\frac{\Delta_b}{2d_b}} \quad (4)$$

d_b is the distance between the centers of the contact disks. With this estimation, the following relation can be obtained:

$$\frac{R_{eff}}{R_{theor}} = \frac{R_1+R_2}{R_1} = 1 + \frac{d_b^2}{2\Delta_b l}\left[\frac{1-\frac{\Delta_b}{d_b}}{1+\frac{\Delta_b}{2d_b}}\right] \qquad (5)$$

It should be noted that this expression is an empirically derived approximation from numerical finite element calculations.

2.2 Current constrictions in modern porous mixed ionic electronic conducting electrodes

The combined electrolyte and AC current constriction resistance is usually determined by impedance spectroscopy. For increased active area technological relevant electrodes are porous and mixed ionic electronic conducting (MIEC). The first obvious choice is to have one electrode material, which satisfies all technological relevant needs. In such cases the whole electrode/electrolyte interface is active and frequency independent. However, a material which satisfies all desirable criteria is rarely found. Therefore, electrodes are often a composite where one material is a very good electronic conductor, while the other material is a good ionic conductor. Such MIEC composite electrodes (either as a microstructured cermet or a coated backbone) will show a frequency dependent serial resistance / current constriction in impedance spectroscopy. As an illustration, we look at a reconstructed solid oxide cell (SOC) Ni:YSZ composite electrode, which is examined as a case study further within the present paper. The situation is sketched in figure 2. The serial resistance is usually determined as the high frequency interception with the real axis in impedance spectroscopy. As illustrated in figure 2, the AC current chooses, as always, the easiest path, which at these conditions is through the highly electrical conductive Ni phase and through the interfacial double layer capacitance. In contrast, at low frequency the capacitive AC current is small compared to the DC current, which flows through the electrode electrochemical reaction, implying that the reaction path is that of a transmission line where the ionic conductive YSZ network is utilized. Thus, the current flow at high and low frequencies and hence the current constriction (effective serial resistance) are different from each other. Composite based electrodes may be better in terms of polarization resistance, but they will always have a higher electrode/electrolyte current constriction than MIEC material based electrodes, which at all frequencies utilize the whole electrode/electrolyte contact area.

3. Experimental

3.1 Finite-Element-Method calculations

For numerical calculations, the finite-element-method (FEM) was used. The program COMSOL Multiphysics® 5.2 was used for all FEM calculations controlled programmatically through the LiveLink for Matlab interface. The program ScanIP 7.0 (Synopsys Inc.) was used to convert the segmented 3D voxel data to tetrahedral meshes. To ensure a smooth mesh transition when varying the electrolyte thickness the variation in the electrolyte thickness was applied to the voxel data and then subsequently remeshed using identical meshing parameters.

Since the problem we want to solve is linear (Ohm's law) we can in principle assign the working electrode and counter/ground electrode arbitrary potentials. However, for practical convenience the working electrode was assigned the potential of 1 V, while the counter/ground was assigned the potential of 0 V. This is illustrated in figure 3. All other external boundaries were set to be insulating. For calculation of the corresponding potential distribution φ, the Laplace equation is solved:

$$\nabla^2\varphi = 0 \qquad (6)$$

The associated current I for a given conductivity σ can be calculated by a boundary integration of the local current densities of e.g. the counter electrode with the area A:

$$I = \int_A -\sigma\nabla\varphi \cdot dA \qquad (7)$$

And thus it is possible to calculate the resistance as the potential difference divided by the associated current flowing through the geometry R=ΔV/I. The used conductivity of Ni and YSZ and the temperature dependency used in the modelling of 3D reconstructions are given in table 1.

3.2 Alignment and representative volume of 3D reconstructions:

To accurately evaluate the effect of the electrolyte thickness it is important that the electrolyte/electrode interface in the data is parallel to the planes where the potential boundary conditions are applied and the current is evaluated. The raw 3D reconstruction of the electrode/electrolyte assembly was slightly tilted compared to this desired orientation. In order to align the electrode/electrolyte interface the following alignment procedure was followed. The coordinates of the first Ni particle encountered, when going from the electrolyte through the electrode along the voxel grid axis, was recorded. These coordinates form a point cloud in 3D space, which was fitted with a plane by least squares with removal of the largest outliers. The entire 3D dataset was then aligned and resampled such that the fitted electrolyte plane had the desired orientation.

To estimate the representative volume size for the present calculations the following procedure was performed. The electrode/electrolyte interface was defined as the last voxel grid plane that does not includes a Ni voxel when going from the electrolyte towards the electrode.

Taking this defined interface as one of the sides of a volume with a constant area of 167 μm^2, the thickness of the electrode was varied as shown in figure 4A. From the figure, it is seen that when the electrode thickness is greater than approximately 5 μm, the results are invariant and can thus be considered representative. Next the electrode thickness was kept at a thickness of 6.89 μm and the electrolyte/electrode area was varied as shown in figure 4B. It is seen that, when the area is larger than around 60 μm^2, the results become invariant and can therefore be considered representative. Based on these investigations an electrode thickness of 6.89 μm and an area of 167 μm^2 was chosen and used as a representative volume for the calculations in section 4.3. The electrode thickness of 6.89 μm was here set as the location of the electrode / electrolyte interface (zero electrolyte thickness in figure 8). For the slicing through the electrode/electrolyte assembly in section 4.4 an area of 167 μm^2 was used.

To evaluate the effect of the mesh on the calculated the results the standard electrode volume of 6.89 x 12.96 x 12.95 μm (191 x 359 x 277 voxels) was remeshed with varying levels of mesh refinement and the current was simulated. The number of tetrahedra was thus varied in 8 steps between $6.02 \cdot 10^6$ and $13.8 \cdot 10^6$ resulting in a relative standard diviation (std.) of just 0.23 % with no significant correlation between the result and the number of tetrahedra. The meshing settings corresponding to $7.33 \cdot 10^6$ tetrahedra was chosen for all subsequent meshing tasks.

3.3 Characteristics of studied electrode/electrolyte assembly

The studied Ni:YSZ SOFC anode is from a cell, which briefly described has been prepared by tapecasting of the Ni:YSZ support onto which the Ni:YSZ anode was deposited by spraying followed by spraying of a YSZ electrolyte layer. This three layered structure (half cell) was co-sintered in air after which a LSM:YSZ composite cathode was applied onto the half cell and sintered at an elevated temperature in air. The prepared cell was tested in a similar way as described in [13], but only with an initial characterization of the cell with IV curve and impedance recorded at 850 ºC, 800 ºC and 750 ºC. Subsequently to this characterization, the cell was cooled down to room temperature in an atmosphere of 9% H_2 in N_2. The impedance response without and with inductance correction, via Kramers-Kronig relations, of the studied cell at 750 ºC is shown in figure 5A. From the spectrum it is possible to extrapolate and make an estimation of the cell serial resistance $R_s \sim 0.1$ Ωcm^2. An image of the cell cross section is shown in figure 5B, from which, it is also possible to see the volume, which has been used for the FIB/SEM 3D tomography reconstruction. Finally, it is possible to see that the thickness of the YSZ electrolyte layer is 10 μm.

3.4 Reconstruction via FIB / SEM nanotomography:

The sample was embedded in epoxy and polished to reveal a crossection through all layers. 3D image data of the sample was obtained by FIB/SEM nanotomography using a Carl

Zeiss 1540 XB microscope. Images were acquired simultaneously at 2 kV using both the SE2 (Everhart- Thornley) and the InLens detectors (through-the-lens type) at an image plane resolution of 36.09 (perpendicular to the electrolyte) x 36.09 nm and a slice thickness of 46.74 nm. The FIB slicing probe was set at 2 nA. Image segmentation was performed by 2D thresholding in the intensity space of both detectors. Segmentation errors due to uncommon imaging artefacts were corrected by hand.

4. Results

Initially, results on ideal geometries are presented. This is done to illustrate possible scenarios and what to expect as support for the interpretation of the calculated results on reconstructed electrode/electrolyte assemblies.

4.1 Current constriction resistance on ideal model systems and the effect of varying the electrolyte layer thickness

For illustration of the effect of current constriction and the effect of varying the electrolyte layer thickness L, calculations were performed on the simple geometries as shown in the inset figure A) and B) + C) in the upper left corner of figure 6. The five contact points on each side of the electrolyte layer are supposed to reflect the current constriction at electrode/electrolyte interfaces. At first, we look at the current constriction from one electrode as a function of electrolyte layer thickness. This is done by setting the opposite electrode as if there were no current constriction (whole area active). The result is seen in figure 6 as case A). For thick electrolytes, the area specific resistance (ASR) varies linearly with electrolyte layer thickness as the theory for a constant electric field predicts ($ASR=\rho \cdot L$). However, as the electrolyte thickness is reduced the onset of a deviation from a linear relationship is seen and for the thickness approaching zero, the resistance also approaches zero, since this eventually will correspond to a short circuit. The extrapolation of the linear relationship for thick electrolytes to zero thickness gives an offset for the y-axis interception. This corresponds to the current constriction resistance associated with the given electrode/electrolyte assembly.

Now the next step is to look at the current constriction of two electrode/electrolyte assemblies as a function of electrolyte thickness. This is also seen in figure 6 as case B). For thick electrolytes we see the same trend as previously with a linear relationship. The slope for these two cases A) and B) are the same as the electrolyte resistivity ρ is unchanged. Extrapolation of the linear regime to zero gives approximately a twice as high y-axis offset as for case A), which simply corresponds to the current constriction resistance of two electrodes instead of one electrode as for case A). However, a different response is seen for the sub 10 μm regime with the resistance approaching infinity instead of zero as the electrolyte layer thickness

approaches zero. This behavior is due to the onset of lateral currents within the electrolyte layer, and the result is a minimum in resistance as a function of electrolyte layer thickness. A closer look reveals, that the behavior of the resistance approaches infinity as the electrolyte thickness approaches zero is only valid for the case, where the contact points of the two electrodes are not opposite to each other (see figure 6 case B). On the other hand, if there is an overlap of the contact points as the electrolyte thickness approaches zero we get a response, which is a combination of the two responses A) and B) discussed previously. This is shown in figure 6 as case C). This can be understood as follows, when the electrolyte thickness L is reduced the onset of lateral currents takes place and on a further reduction in electrolyte layer thickness it will eventual be more favorable for the current to avoid the lateral currents in the electrolyte layer and instead only utilize the electrode area, which have an overlap with the opposite electrode contact points (reduction in active area). This will eventually on a further reduction in electrolyte thickness lead to a short circuit. In these considerations it is only the geometry (primary current distribution), which determines the current and thus the minimization of the overall resistance. In practical cases there will be other resistance contributions such as electrode reaction resistances and/or interfacial charge transfer resistances at the electrode/electrolyte contact points (secondary current distribution). Adding a relatively small contact resistance to the electrode/electrolyte interfaces means that the utilization of a smaller area in case C) becomes less favorable. It is now a competition between minimizing the primary and secondary current contributions. This is also illustrated in figure 6 for case D), where a small contact resistance of $5*10^{-4}$ Ωcm^2 has been added. For thick electrolytes it is seen to have a small impact on the overall resistance. However, when the electrolyte layer thickness approaches zero a response similar to case C) is seen, where a local minimum in ASR occurs before zero electrolyte thickness. However, upon the introduction of a contact resistance the situation of utilizing a smaller area becomes significantly less favorable. This is even more evident, when the contact resistance is further increased to 10^{-3} Ωcm^2 in case E), where the onset of the resistance approaches zero, as the thickness of the electrolyte layer is approaching zero, is absent. Thus, for most practice cases it is expected that lateral currents within the electrolyte layer are more favorable to maintain a utilization of the whole electrode/electrolyte areas/interfaces to minimize the resistance associated with the secondary and tertiary current distributions. The results with the presence of a contact resistance is phenomelogical similar to case C in figure 6, but with the local resistance maxima shifted to thinner electrolyte thicknesses as the contact resistance is increased.

4.2 Current constriction resistance and effect of slicing through the electrode/electrolyte assembly

The previous approach in section 4.1 assumes that the location of the interface is known and well defined. Furthermore, in composite electrodes such as Ni:YSZ the Ni phase is dominating in terms of conductivity. This implies, that it is the interface between Ni electrode particles and the YSZ electrolyte material, which is active in the impedance spectroscopy

determined serial resistance as discussed in section 2.2 (AC current constriction resistance). The DC current constriction resistance is not so easily determined as the ionic conducting part of the composite electrode and the electrolyte is usually the same material (typically YSZ). Thus, it is challenging to distinguish between electrode and electrolyte YSZ. A possible approach is to slice through the electrode/electrolyte assembly as illustrated in the ideal situation in figure 7. In this situation, the porous electrode structure is modelled as columns as in [14-16]. From figure 7 it is seen, that slicing through the assembly there are two regions with different slopes along with a transition zone. The slope is equal to the resistivity, which is larger in the electrode phase compared to electrolyte phase due to the presence of porosity. Extrapolation of the linear regimes in the electrode and electrolyte phases gives an interception, which would be the location of the interface if no current constriction existed. However, current constriction resistance shifts the whole linear regime of the electrolyte phase to higher resistances and therefore also the interception of the extrapolated linear regimes of the electrode and the electrolyte phases. From the onset of non-linearity of the electrode phase it is possible to make an estimation of the interface location and the current constriction resistance of the electrode/electrolyte assembly as illustrated in the inset of figure 7. The advantage of such an approach is that no assumptions/definition of the interface is needed.

4.3 AC current constriction resistance of a Ni:YSZ SOFC anode

Figure 8 shows the simulated AC current constriction resistance for the reconstructed Ni:YSZ composite SOFC anode. Zero electrolyte thickness is defined as the thickness where the first Ni particle penetrates the electrolyte plane. Unlike the ideal interface situation in figure 6 (case A), the deviation from linearity is only weakly observed as the interface is approached. Nonetheless, it is possible from the offset of the y-axis to estimate the AC current constriction resistance to 8 $m\Omega cm^2$. However, it is also clear that this value is dependent on where the electrode/electrolyte interface is defined. Thus, the electrode/electrolyte interface definition is critical and the relatively weak deviation from linearity in figure 8 is probably an indication, that the interface is to some extent smeared out.

4.4 AC and DC current constriction resistances determined by slicing through the electrode/electrolyte assembly

The results of slicing through the Ni:YSZ electrode / YSZ electrolyte assembly is shown in figure 9. The general trend of these calculations is similar to the one which was observed on the ideal artificial geometry in figure 7. In figure 9A and 9B the Ni and YSZ has been assigned the conductivities specified in table 1. That is, Ni has a superior conductivity compared to YSZ. It is seen, that in the porous electrode the ASR is very low and upon going from the electrode phase to the electrolyte phase there is an abrupt increase in ASR, which is due to the significantly

poorer conductivity of the YSZ electrolyte phase and the loss of Ni percolation between the two end planes. This relatively sharp increase in ASR specifies the AC current constriction electrode/electrolyte interface. The location of this interface at 6.60 μm is different from the one used in figure 8 at 6.89 μm. The discrepancy is due to the first Ni particle encountered not having a connection to the rest of the Ni network. From figure 9B an AC current constriction resistance of 6.5 $m\Omega cm^2$ can be determined, which is slightly less than 8 $m\Omega cm^2$ as determined from the figure 8. This is due to the difference in location of the AC interface.

Figure 9C and 9D show the situation where only YSZ is active. The trends are in accordance with expectations according to figure 7. From the transition zone between the porous electrode and dense electrolyte it is possible to estimate the DC current constriction ASR as illustrated in section 4.2, where the ideal artificial situation was studied. The data points of the thinnest electrode thicknesses are somewhat off the fitted line. This is believed to be due to variations in the microstructure between these data points (local electrode current constriction) due to the smaller conductive phase fraction. For the electrode thickness approaching zero, the tortuosity factor has to approach one. Therefore as the electrode thickness is increased from zero, the tortuosity will increase initially until a certain thickness is reached after which, the tortuosity factor will level out upon further increase in electrode thickness. When a certain volume is obtained the results will be representative and a constant tortuosity is seen upon further thickness and thus volume increase. From the transition region between the electrode and the electrolyte phases, which are magnified in figure 9D, the DC current constriction ASR can be estimated to roughly 11 $m\Omega cm^2$. The location of the DC current constriction interface at 5.38 μm is significantly different from the AC current constriction interfaces determined in figure 9B at 6.60 μm and figure 8 at 6.89 μm. Correlation of ASR with phase fractions indicate the DC current constriction interface to be located just before the start of the transition region between the electrode phase and the electrolyte phase. This is in contrast to the AC current constriction interface, which were located just after the transition region in figure 9B or somewhat after the transition region in figure 8.

Finally, figure 9E and 9F represent the situation where all the electrode solid phases (both Ni and YSZ) are active with the conductivity of YSZ provided in table 1. This configuration is included to illustrate the situation which is present in a MIEC material based electrode. As expected a higher density of contact points at the interface results in a significantly lower AC/DC current constriction resistance of 3 $m\Omega cm^2$. Furthermore, it can be seen that the location of the electrode/electrolyte interface at 5.21 μm is very close to 5.38 μm, which was determined for the Ni/YSZ composite DC current constriction case in figure 9D. The higher fraction of active electrode phase (Ni and YSZ) in comparison to the consideration of only the YSZ in figure 9D, is expected to result in a less tortuous microstructure with more alternative pathways and thus a lower dependence on local microstructure variations when zero electrode thickness is approached. For example the data points for thin electrode thicknesses in figure 9F follows the fitted line much better than the case with only YSZ being active in figure 9D.

5 Overall discussion

From the phase fraction data in figure 9, it can be seen that the transition region between the electrode and electrolyte phase is approximately 1 μm. If we define the interface as the encounter of the first Ni particle as explained in section 3.4 and calculate the shortest pathway distance from this interface to the nearest Ni particle within the porous electrode we get a histogram as shown in figure 10A. For comparison an arbitrary cross section within the porous electrode is shown in figure 10B. A clear difference is seen for the two situations. From figure 10A we see a gauss like distribution, which also confirms, that the first Ni particles we encounter when going from the electrolyte phase to the electrode phase is likely to be nonpercolated. This explains the different determined interface locations observed in figure 8 and figure 9. In addition, the histogram in figure 10A is also in line with a transition region of around 1 μm.

The AC current constriction interface therefore seems to be associated with the position of the first Ni percolated particle encountered when going from the electrolyte phase towards the electrode phase, which is closely related to the electrode Ni phase fractions approaching zero. This is unlike the DC current constriction resistance interface, which from the results of figure 9 seems to be related to the onset of the YSZ interface transition when going from the electrode towards the electrolyte. That the DC current constriction interface location is different from the AC current constriction interface may be understood as follows. As the decrease in electrode porosity begins an increase in YSZ phase fraction starts, which enables the current to spread out and diminish the resistance associated with current conduction. Thus, there will be a drop in ASR (the slope) when the YSZ phase fraction increases, which may be interpreted as the DC current constriction resistance. In summary, upon impedance acquisition of a MIEC composite electrode not only will the serial resistance in principal change, the location of the interface may also change, when for example going from high frequencies to low frequencies. This is unlike an MIEC material based electrode, where both the current constriction resistance and the electrode/electrolyte interface location is frequency independent. That a frequency dependent current distribution influences the usual way of determining the polarization resistance as $Rp=Z(freq. \rightarrow \infty) - Z(freq. \rightarrow 0)$ in impedance spectroscopy is not new and has been discussed before for various situations [17-19].

The relatively smeared out interface is probably a characteristic of the preparation method and the slurries used for tape casting and spraying. It is e.g. expected, that a finer micro structured electrode and use of for example tape casting exclusively will result in a sharper transition and thus a sharper interface. The theoretical electrolyte resistance $R_{theory}(YSZ)$ with the parameter values of table 1 for an electrolyte thickness of 10 μm is 48 $m\Omega cm^2$. This means that the determined AC current constriction resistance of the anode/electrolyte interface of 6.5 $m\Omega cm^2$ is 14% of the $R_{theory}(YSZ)$. The effective electrolyte resistance was experimentally estimated to be ~ 100 $m\Omega cm^2$ in section 3.1. This means, that the cathode/electrolyte current constriction resistance should be 45 $m\Omega cm^2$, which is a very high value and thus it seems very unlikely. It is more likely that there are some losses associated with current collection in the

experimental test setup. In the used setup a LSM based cathode current collector is used. Use of Au meshes as cathode current collector has been tested in our lab and the results have clearly indicated that the use of a LSM based current collector is not an optimal solution and is associated with some loss. The temperature dependency of the current constriction resistance will be the same as that of the electrolyte material. It implies, that, the relative contribution of the current constriction resistance to the electrolyte resistance will be constant as a function of temperature.

In figure 11A a cross section image of the AC current constriction interface as determined from figure 9A and 9B is shown, while in figure 11B an arbitrary cross section of the electrode is shown. From figure 11A very few Ni particles (white) are seen. From the image in figure 11 it is clear that the assumptions in model a (Kenjo) and b (Fleig) sketched in figure 1 of equal sized, shaped and spaced array of contact points seem somewhat doubtful. Nonetheless, if we use the average area per contact point and distribute the contact points evenly, it is possible to apply the models. This is done in figure 12. In figure 12A the models are applied to the interface in figure 11A, which shows, that both model a (Kenjo) and b (Fleig) results in very high resistances roughly 10 and 30 times higher than the 3D FEM calculations. However, if we use the arbitrary electrode cross section in figure 11B we get the results in figure 12B, which are considerably closer to the 3D FEM calculations in magnitude, but nonetheless not in accordance. These calculations illustrate, that the assumptions in the models a (Kenjo) and b (Fleig) are by far too simple and do not reflect the situation in technological relevant solid state electrodes. For accurate estimations of losses due to current constriction, FEM calculations on representative 3D reconstructions should be performed.

6. Conclusions

Possible scenarios in respect to current constriction resistance were reviewed, explored and illustrated through numerical finite-element-method calculations. It was illustrated that there is an optimal electrolyte layer thickness, when the electrolyte is sandwiched in between a given set of electrodes (anode and cathode). The optimal electrolyte thickness depends among other things on the microstructural and material characteristics of the employed electrodes. Furthermore, it was shown how it is possible to calculate the current constriction resistance of an individual electrode/electrolyte interface with no prior knowledge about the interface and its location by FEM calculations of slicing through the electrode/electrolyte assembly. This methodology was applied to FIB-SEM 3D reconstructions of a technological relevant Ni:YSZ composite SOFC anode. From these calculations it was possible to separate and determine the high frequency (AC) and low frequency (DC) current constriction resistances. It was found that the area specific AC and DC current constriction was 6.5 $m\Omega cm^2$ and 11 $m\Omega cm^2$ respectively. Finally, it was clearly illustrated that available models with analytical expressions are inadequate in the determination of the current constriction resistance.

Acknowledgement

We gratefully acknowledge Energinet.dk through the ForskEL project "Solid Oxide Fuel Cells for the Renewable Energy Transition" contract no 2014-1-12231 and Department of Energy Conversion & Storage, Technical University of Denmark for financial support.

References

[1] F. Han, R. Mücke, T. Van Gestel, A. Leonide, N.H. Menzler, H.P. Buchkremer, D. Stöver, Novel high-performance solid oxide fuel cells with bulk ionic conductance dominated thin-film electrolytes, Journal of Power Sources. 218 (2012) 157–162. doi:10.1016/j.jpowsour.2012.06.087.

[2] C. Ding, T. Hashida, High performance anode-supported solid oxide fuel cell based on thin-film electrolyte and nanostructured cathode, Energy Environ. Sci. 3 (2010) 1729–1731. doi:10.1039/C0EE00255K.

[3] D. Roehrens, U. Packbier, Q. Fang, L. Blum, D. Sebold, M. Bram, N. Menzler, Operation of Thin-Film Electrolyte Metal-Supported Solid Oxide Fuel Cells in Lightweight and Stationary Stacks: Material and Microstructural Aspects, Materials. 9 (2016) 762. doi:10.3390/ma9090762.

[4] V. Esposito, C. Gadea, J. Hjelm, D. Marani, Q. Hu, K. Agersted, S. Ramousse, S.H. Jensen, Fabrication of thin yttria-stabilized-zirconia dense electrolyte layers by inkjet printing for high performing solid oxide fuel cells, Journal of Power Sources. 273 (2015) 89–95. doi:10.1016/j.jpowsour.2014.09.085.

[5] H. Moon, S.D. Kim, S.H. Hyun, H.S. Kim, Development of IT-SOFC unit cells with anode-supported thin electrolytes via tape casting and co-firing, International Journal of Hydrogen Energy. 33 (2008) 1758–1768. doi:10.1016/j.ijhydene.2007.12.062.

[6] S.A. Barnett, A new solid oxide fuel cell design based on thin film electrolytes, Energy. 15 (1990) 1–9. doi:10.1016/0360-5442(90)90059-B.

[7] S. de Souza, S.J. Visco, L.C. De Jonghe, Thin-film solid oxide fuel cell with high performance at low-temperature, Solid State Ionics. 98 (1997) 57–61. doi:10.1016/S0167-2738(96)00525-5.

[8] T. Kenjo and T. Nakagawa, *J. Electrochem. Soc.*, **143**, L92–L94 (1996).

[9] J. Fleig, J. Maier, in: *Proc. 5th Int. Symp. Solid Oxide Fuel Cells*, U. Stimming, S. C. Singhal, H. Tagawa, W. Lehnert, Editors, p. 1374, The electrochemical Society, Pennengton NJ (1997).

[10] E. Wanzenberg, F. Tietz, D. Kek, P. Panjan, D. Stöver, Influence of electrode contacts on conductivity measurements of thin YSZ electrolyte films and the impact on solid oxide fuel cells, Solid State Ionics. 164 (2003) 121–129. doi:10.1016/j.ssi.2003.08.053.

[11] J. Fleig, H.L. Tuller, J. Maier, Electrodes and electrolytes in micro-SOFCs: a discussion of geometrical constraints, Solid State Ionics. 174 (2004) 261–270. doi:10.1016/j.ssi.2004.07.035.

[12] J.-H. Park and R. N. Blumenthal, *J. Electrochem. Soc.*, 136, 2867–2876 (1989).

[13] J. Nielsen, A. Hagen, Y.L. Liu, Effect of cathode gas humidification on performance and durability of Solid Oxide Fuel Cells, Solid State Ionics. 181 (2010) 517–524. doi:10.1016/j.ssi.2010.02.018.

[14] J. Nielsen, T. Jacobsen, M. Wandel, Impedance of porous IT-SOFC LSCF:CGO composite cathodes, Electrochimica Acta. 56 (2011) 7963–7974. doi:10.1016/j.electacta.2011.05.042.

[15] J. Nielsen, J. Hjelm, Impedance of SOFC electrodes: A review and a comprehensive case study on the impedance of LSM:YSZ cathodes, Electrochimica Acta. 115 (2014) 31–45. doi:10.1016/j.electacta.2013.10.053.

[16] J. Nielsen, T. Klemensø, P. Blennow, Detailed impedance characterization of a well performing and durable Ni:CGO infiltrated cermet anode for metal-supported solid oxide fuel cells, Journal of Power Sources. 219 (2012) 305–316. doi:10.1016/j.jpowsour.2012.07.031.

[17] J. Fleig, J. Maier, The Influence of Current Constriction on the Impedance of Polarizable Electrodes Application to Fuel Cell Electrodes, J. Electrochem. Soc. 144 (1997) L302–L305. doi:10.1149/1.1838076.

[18] T. Kenjo, Y. Kanehira, Influence of the local variation of the polarization resistance on SOFC cathodes, Solid State Ionics. 148 (2002) 1–14. doi:10.1016/S0167-2738(02)00119-4.

[19] J. Nielsen, T. Jacobsen, Current distribution effects in AC impedance spectroscopy of electroceramic point contact and thin film model electrodes, Electrochimica Acta. 55 (2010) 6248–6254. doi:10.1016/j.electacta.2009.11.028.

Figure and table captions

Figure 1: Geometry of contact points at solid electrolyte / porous electrode interfaces in **a)** Kenjo et al. model [8] **b)** Fleig et al. model [9].

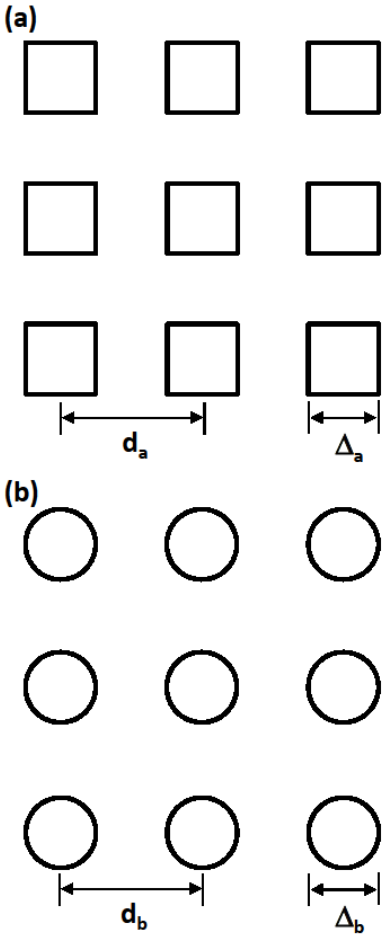

Figure 2: AC and DC current distributions in a Ni:YSZ composite solid oxide cell electrode. The DC current distribution corresponds to a transmission line response.

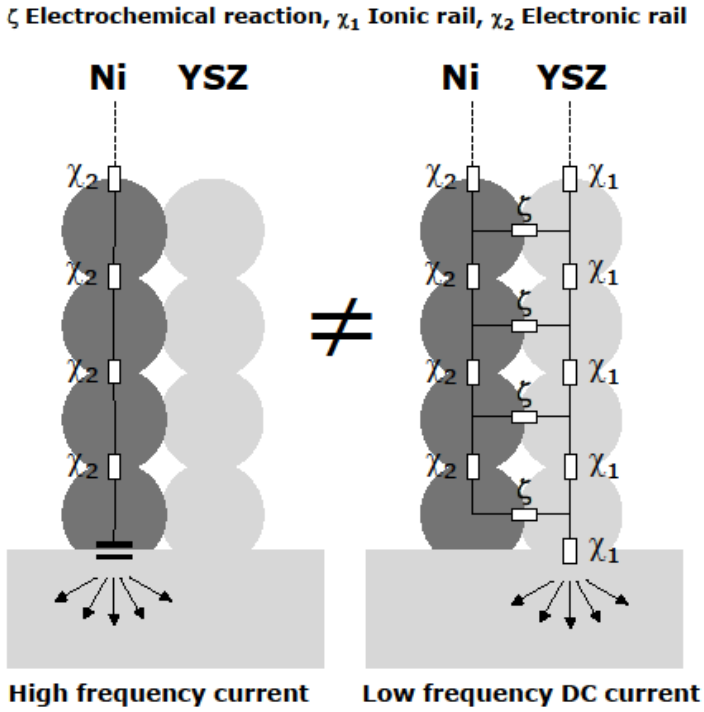

Figure 3: Example of model setup and the resulting potential distribution in a 3D reconstructed porous Ni:YSZ electrode / dense YSZ electrolyte assembly.

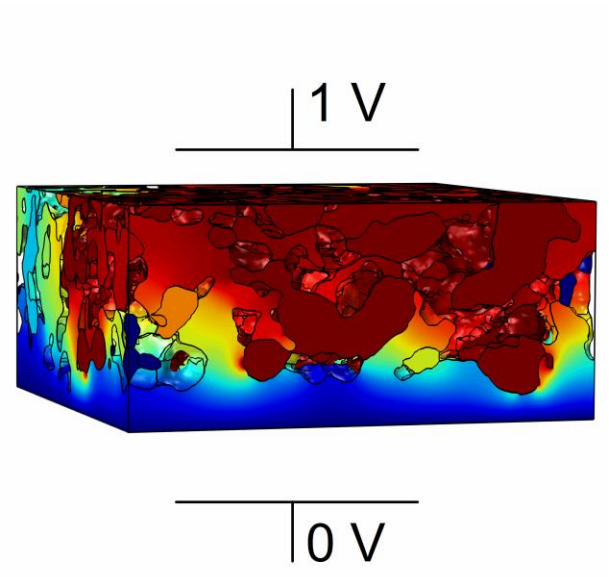

Figure 4: A) Current as function of electrode thickness for an electrolyte/electrode interface with an area of 167 μm^2. **B)** Electrode/electrolyte area specific current through an electrode volume where the electrode thickness is kept constant at 6.89 µm and the electrode/electrolyte area is varied. The average current value (red dashed line) is normalized to 1 with a standard deviation of S_{dev}=0.031.

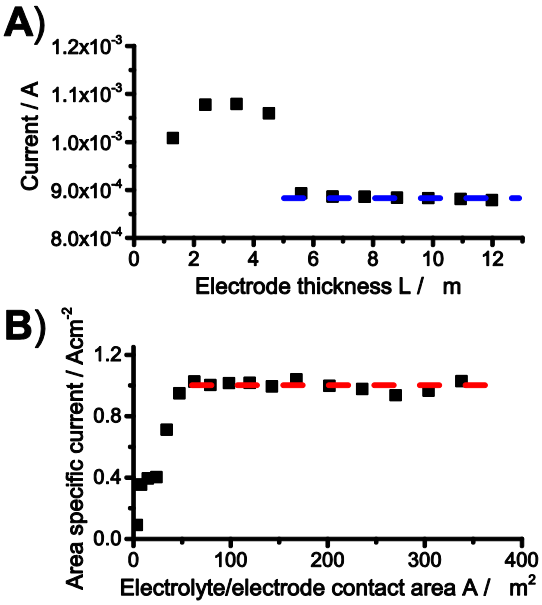

Figure 5: A) Impedance spectrum uncorrected and inductance corrected via the use of Kramers-Kronig relations of studied AS-SOFC at 750°C with air as oxidant and 20% humidified hydrogen as fuel. B) Cross section of the studied SOFC, where the trench resulting from the FIB/SEM tomography 3D reconstruction can be seen.

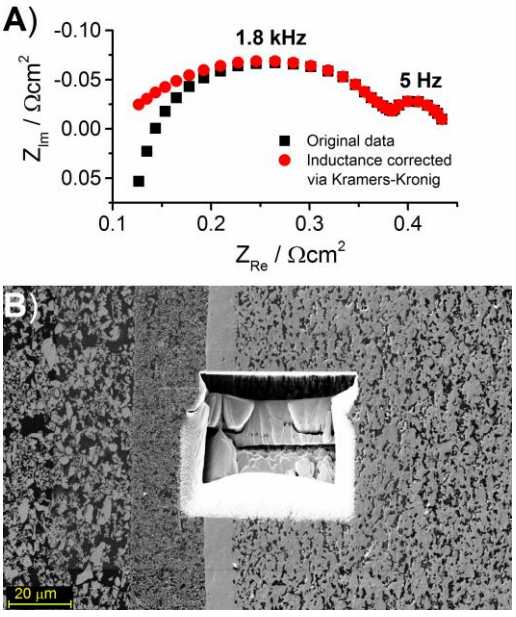

Figure 6: Ideal geometry used for calculations of possible current constriction resistance scenarios as a function of the electrolyte thickness. The circle areas represent electrode/electrolyte contact points, which are assigned a given potential. **A)** The case with 1 electrode. **B)** The case with an electrolyte layer, which is sandwiched in between to electrodes. In this case there is no overlap between the electrode/electrolyte contact points of the two electrodes, when looking from the top and down through the whole assembly. **C)** The case where there is an overlap between the electrode/electrolyte contact points of the two electrodes, when looking from the top and down through the whole assembly. The situation is otherwise similar to case B. **D) +E)** is similar to case C, but with the exception, that the electrode/electrolyte contact points have been assigned a contact resistance to reflect a secondary potential distribution.

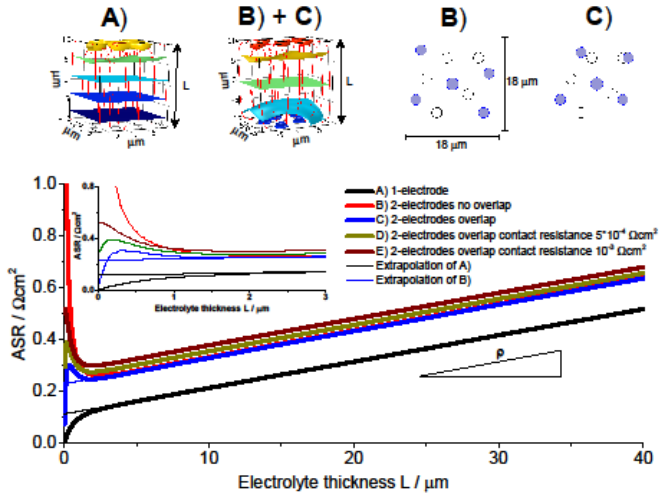

Figure 7: Ideal geometry of a porous electrode / electrolyte assembly and the result on the area specific resistance of slicing through the assembly.

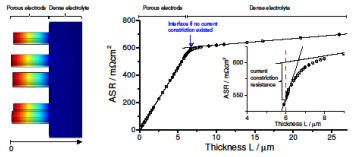

Figure 8: Calculated AC area specific resistance (ASR) as a function of electrolyte thickness for a NI:YSZ SOFC anode, when the anode/electrolyte interface is defined as the encounter of the first Ni particle when going from the electrolyte phase to the electrode phase.

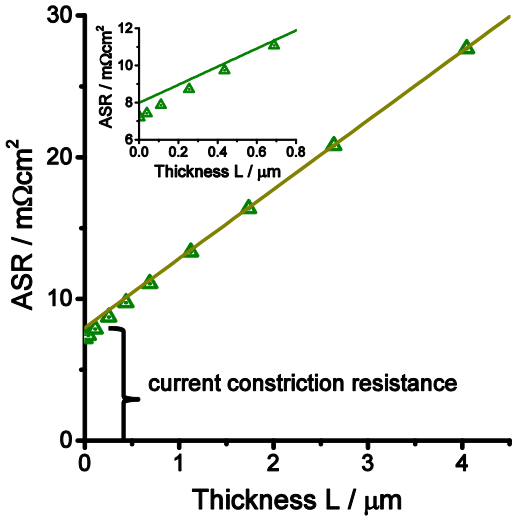

Figure 9: FEM calculated results on the area specific resistance (ASR) as a function of slicing through a Ni:YSZ electrode and YSZ electrolyte 3D reconstructed assembly. **A) + B)** The Ni and YSZ phases have been assigned the conductivities specified in table 1. **C) + D)** Only the YSZ phase is active and has been assigned the conductivity specified in table 1. **E) + F)** Both the Ni and the YSZ phase has been assigned the conductivity of YSZ specified in table 1.

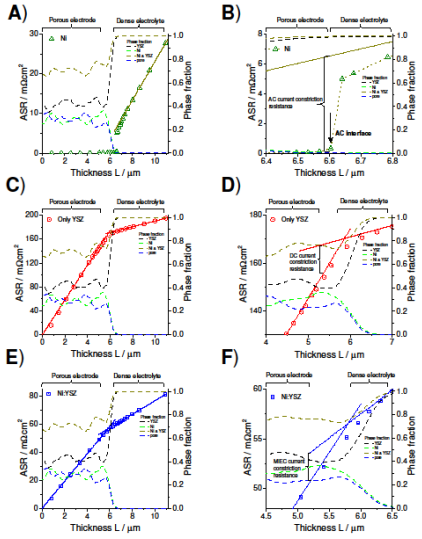

Figure 10: A) Distance of the shortest pathway from the electrode/electrolyte interface to a Ni particle, when the interface is defined as the encounter of the first Ni particle when going from the electrolyte phase to the electrode phase. **B)** Similar calculation performed for a cross section in the middle of the porous electrode.

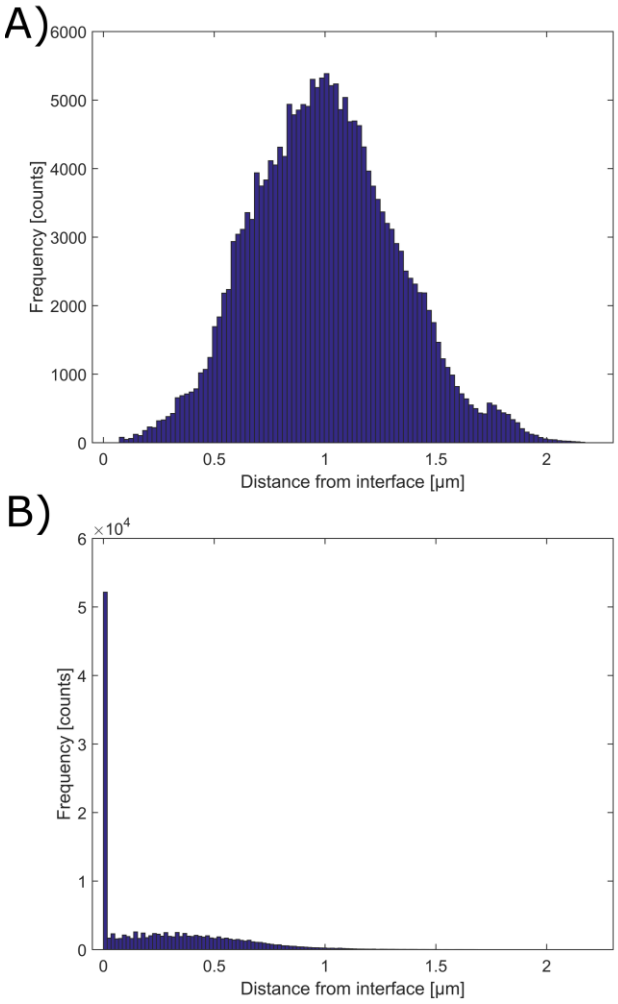

Figure 11: A) Cross section of the AC current constriction interface at 6.60 μm in figure 9A+9B. **B)** Arbitrary electrode cross section perpendicular to the electrode thickness direction. The white part is Ni, the grey part YSZ and the black part porosity. The whole area is 167 μm^2.

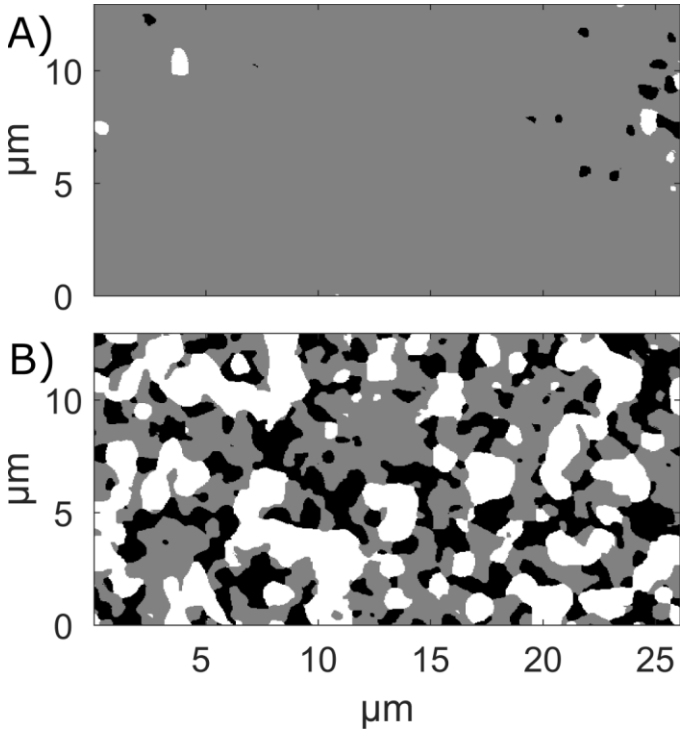

Figure 12: Comparison of the calculated combined current constriction and electrolyte resistance of the AC interface at 6.60 μm in figure 9B with models. **A)** Comparison with models applied to the interface of figure 11A with the image determined models parameters d_a=d_b= 4.88 μm, Δ_a=0.394 μm, Δ_b=0.445 μm. **B)** Comparison with models applied to the interface of figure 11B with the image determined models parameters d_a=d_b= 4.88 μm, Δ_a=0.394 μm, Δ_b=0.445 μm.

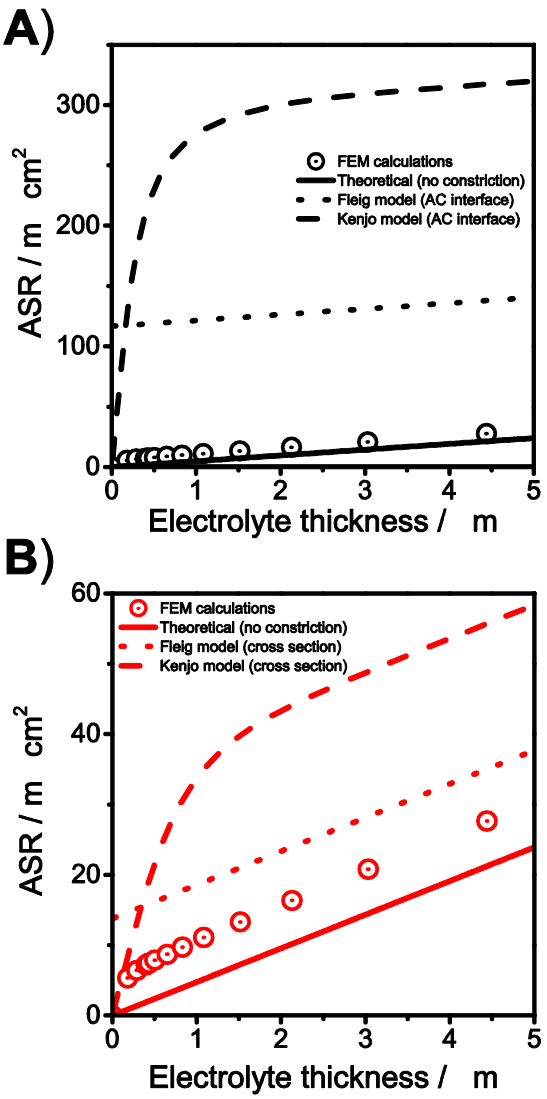

Table 1: Material properties and temperature used in the FEM calculations.

Parameters used in the modelling		
$\sigma_{Ni} = 100000\ [S/m]$	$\sigma_{8YSZ} = 16300 \cdot exp\left(\frac{-9168}{T}\right)\ \left[\frac{S}{m}\right]$ [12]	T = 1023 K